Science Bulletin 64 (2019) 1667–1674

Contents lists available at ScienceDirect

Science Bulletin

journal homepage: www.elsevier.com/locate/scib

Science Bulletin
www.scibull.com

Article

Heptanuclear brucite disk with cyanide bridges in a cocrystal and tracking its pyrolysis to an efficient oxygen evolution electrode

Jian-Qiang Zhao [a], Dandan Cai [a], Jun Dai [a], Mohamedally Kurmoo [c], Xu Peng [b,*], Ming-Hua Zeng [a,b,*]

[a] Key Laboratory for the Chemistry and Molecular Engineering of Medicinal Resources, Department of Chemistry and Pharmaceutical Sciences, Guangxi Normal University, Guilin 541004, China
[b] Hubei Collaborative Innovation Center for Advanced Organic Chemical Materials, Ministry of Education Key Laboratory for the Synthesis and Application of Organic Functional Molecules, College of Chemistry and Chemical Engineering, Hubei University, Wuhan 430062, China
[c] Institut de Chimie de Strasbourg, CNRS-UMR7177, Université de Strasbourg, 67070 Strasbourg Cedex, France

ARTICLE INFO

Article history:
Received 7 July 2019
Received in revised form 14 August 2019
Accepted 6 September 2019
Available online 13 September 2019

Keywords:
Cobalt disk clusters
Thermogravimetry-mass spectrometry
Pyrolysis tracking
Core-shell nanostructure
Oxygen evolution reaction

ABSTRACT

The development of efficient oxygen evolution reaction (OER) catalysts is still lacking in exploration of the mechanism of controlled pyrolysis of precursors among new material platforms. Here, a novel Co-based coordination molecular cluster has been first introduced as precursor to obtain metallic cobalt core shelled by N-doped carbon (Co@NC) structure which operates as an oxygen evolution electrode. Specifically, a new cocrystal compound, $[Co^{II}_7(\mu_3\text{-}CN)_6(mmimp)_6]$ $[Co^{II}Cl_3N(CN)_2]\cdot 3CH_3OH$ (**Co_{7+1}**, mmimp = 2-methoxy-6-((methylimino)-methyl)phenol), was isolated consisting of Brucite disks of cobalt where the usual bridging μ_3-OH is replaced by μ_3-CN produced by the *in-situ* decomposition of dicyanamide ($N{\equiv}C\text{-}N\text{-}C{\equiv}N^-$). The cobalt atoms are bonded through the nitrogen atom of the cyanide. Remarkably, time dependent thermogravimetric-mass spectrometry (TG-MS) analysis was utilized to track its pyrolysis process. It allowed us to propose a possible formation process of the Co@NC structure from **Co_{7+1}**. Interestingly, an extremely superior OER electrode is optimized for Co@NC-600 having the lowest overpotential of 257 mV at 10 mA/cm^2 in 1 mol/L KOH solution. The present study pins down the importance of clusters of transition metals on realizing distinct nanostructures operating as highly efficient OER electrocatalyst.

1. Introduction

The construction of material systems through precise chemical synthesis and design in molecular level is a unified dream of chemists and materialists [1–5]. As a hub for energy conversion, electrocatalytic materials are impetus in renewable energy conversion with intriguing applications [6–10]. Therefore, how to precisely regulate the electrocatalyst by chemical control has attracted much attention [11–14]. Among electrocatalytic materials, nanocomposites have demonstrated fascinating advantages and made important progress, especially the as-resulted core-shell nanostructures with synergic effect on high surface areas and electroactive sites [15–18]. Of note, metal–organic frameworks (MOFs) and simple organic-inorganic composites as precursors under proper thermal decomposition are an effective way to prepare electrocatalytic materials with core-shell nanostructures [18–23]. Coordinative cluster has displayed signs of success as potential precursor, with outstanding advantage for achieving subtly regulation on precursor structure through control on the number and kinds of metal ions, metal ion coordination geometry, peripheral ligand, inner bridge ligand, and inter/intra-cluster interaction. Compared with MOFs, the 0D coordination clusters are isolated molecular where the metal core is well surrounded by multiply peripheral ligands. The simultaneous carbonizing of the peripheral ligands during pyrolysis of the cluster promotes the effective carbon cladding and segregation of the metal core, avoiding interference from framework connection leading complicated pyrolysis. In addition, the existence of inner bridge in cluster, like CN^-, CSN^-, N_3^- and others, provide additional chance to induce *in-situ* N-doping, which is beneficial to improvement of electrocatalytic activity [24–26]. However, studies on the precursors of coordination molecular clusters have yet not been reported. Meanwhile, although pyrolysis has been used as a general method for the preparation of electrocatalytic materials, the mechanism of its pyrolysis process has been few studied systematically [27,28]. In this regard, it is urgent to explore and track the mechanism of pyrolysis process, as well as to design a precursor at the molecular

* Corresponding authors.
E-mail addresses: pengxu@hubu.edu.cn (X. Peng), zmh@mailbox.gxnu.edu.cn (M.-H. Zeng).

https://doi.org/10.1016/j.scib.2019.09.013
2095-9273/

level to achieve control and optimization of derivative electrocatalysts.

In our previous work, we have been interested in designing different types of MOFs accurately, and finally realized their functional regulation through post-synthesis modification, such as catalysis, conduction and magnetism [29–31]. Furthermore, we have been engaged in the assembly process and mechanism of coordination molecular clusters and their post-synthesis modification or thermal transformation regulation [32–34]. For some special systems, reasonable design and controlled synthesis can be implemented to control the formation of different internal bridges, different metal ions, complex counter ions and co-crystal clusters [35–37]. In particular, a step-by-step assembly process at room temperature was found when Schiff bases were used as the key chelating ligands, which led to co-crystal heptanuclear disk clusters starting from the Ni_1 via Ni_2, Ni_4 and Ni_{7+1} intermediate species [38]. Driven by above mentioned experience, we recently design a 3-MeOsalophen-ligated cobalt complex as a precursor to obtain a Co@CoO_x-NC core-shell nanostructures with decent oxygen evolution reaction (OER) performance [39]. Therefore, these work bases inspire us to investigate the pyrolysis process of well-designed coordination molecular clusters to obtain a core-shell nanostructure with high electrochemical activity.

In this work, we have chosen the N, O-double chelating Schiff base ligand to design and synthesis a brucite cationic disk Co_7 cluster with discrete $[CoCl_3N(CN)_2]^{2-}$ anion. And for the first time, the introduction of the μ_3-CN^- inner bridge was achieved by *in-situ* decomposition of dicyanamide ions under solvothermal reaction. Interestingly, the rarely observed μ_3-CN bonded through the nitrogen was the bridging ligand at the core of the disk. However, thermal analysis proved to be more interesting with the observation of nanoparticles consisting of cubic cobalt core and N-doped carbon (Co@NC). Moreover, TG-MS technique was used to study the pyrolysis process and revealed the substituents on the ligand and be cleaved to generate a large number of active sites promoting the polymerization and retention of the organic fragments for forming the core–shell nanostructure. Here, we detail the exceptional properties and provide evidence of the above conclusion.

2. Experimental

2.1. Synthesis of Co_{7+1}

$CoCl_2{\cdot}6H_2O$ (1 mmol, 0.238 g) and $NaN(CN_2)$ (1 mmol, 0.089 g) was added to a solution of the Hmmimp (1 mmol, 0.165 g) in CH_3OH (15 mL). Then 0.1 mL triethylamine was added and the mixture was stirred for 10 min before being placed in a 23 mL Teflon-lined autoclave and heated at 80 °C for 2 d. The autoclave was then cooled over a period of 3 h at a rate of 20 °C/h, and the dark green crystals of **Co_{7+1}** were collected by filtration, washed with CH_3OH and dried in air. Yield (based on Co): ca. 38.7%. Anal. calcd. (%) for $Co_8C_{66}H_{76}Cl_3N_{15}O_{16}$: C, 41.13; H, 4.00; N, 10.98. Found (%): C, 41.08; H, 4.06; N, 10.95. IR (cm^{-1}): 3447(w), 2923(w), 2167(s), 1641(s), 1455(s), 1307(w), 1218(s), 1074(w), 1018(w), 960(w), 852(w), 743(s), 636(w), 484(w).

2.2. Synthesis of Co@NC nanomaterials

To obtain the resulting catalysts, the as-prepared precursor (**Co_{7+1}**) was annealed in Ar at different temperatures (500, 600, 700, and 800 °C, respectively) for 2 h with a ramping rate of 2 °C/min. Finally, the black products were washed with deionized water and dried at 80 °C overnight. The resulting catalysts were labeled as Co@NC-500, -600, -700, and -800, respectively.

2.3. X-ray crystallography

Single crystals of compound were collected on a XtaLAB Synergy with graphite monochromated Mo Kα radiation (λ = 0.71073 Å) at 100(2) K. The intensity data were corrected for Lorentz and polarization effects (SAINT), and empirical absorption corrections based on equivalent reflections were applied (SADABS). The structures were solved by direct method and refined on F^2 by full-matrix least-squares method with SHELXL-2014 program package [40]. All non-hydrogen atoms were refined with anisotropic thermal parameters, and the hydrogen atoms of organic ligands were generated theoretically onto the specific carbon atoms and refined isotropically with fixed thermal factors. The crystallographic details are provided in Table S1a (online), and selected bond lengths and angles are given in Table S1b (online). Crystallographic data for the structural analyses have been deposited at the Cambridge Crystallographic Data Centre, reference number 1893855 for **Co_{7+1}**.

2.4. Electrochemical measurements

The electrochemical tests were carried out in a conventional three electrode electrochemical cell by using a CHI760E. The electrochemical impedance spectroscopy (EIS) measurements were carried out by applying Gamry reference 600 instrument. A saturated silver chloride electrode (SSCE) and carbon rods were used as the reference electrode and the counter electrode, respectively. The preparation of the working electrode was performed as described below: carbon paper (1 cm × 1 cm) was utilized as working electrode to reach a high catalyst loading. A 3 mg catalyst and 500 μL ethanol dispersion solution were mixed well by ultrasonicating for 20 min. Then, the uniform suspension was dropped on carbon paper and left to dry in infrared lamp (this yielded an approximate catalyst loading of 1.6 mg/cm^2 on carbon paper). Electrochemical measurements of catalysts were measured in 1 mol/L KOH solution (pH 14) after purging the electrolyte with O_2 gas for 30 min. All tests were carried out at room temperature and presented without iR compensation. The potential, measured against a SSC electrode, was converted to the potential versus the reversible hydrogen electrode (RHE) according to the Nernst equation (E vs. RHE = E vs. SSCE + 0.059 × pH + 0.1989). The Tafel slope was calculated according to the following formula $\eta = b\log(j/j_0)$, where η is the overpotential, b is the Tafel slope, j is the current density, and j_0 is the exchange current density.

2.5. Characterization

Elemental analysis of C, H, and N microanalyses were carried out using an ElementarVario-EL CHNS elemental analyzer. FT-IR spectra were recorded from KBr pellets containing 1% of the compound in the range of 400 ~ 4000 cm^{-1} on a Bio-Rad FTS-7 spectrometer. The thermogravimetric analysis (TGA) was performed using a Pyris Diamond TG/DTA under a constant flow of dry Ar gas at a heating rate of 2 °C/min. The thermogravimetric analysis was performed on a Rigaku Thermo Mass Photo (TG-MS) with a Skimmer type mass spectrometer (MS/EI). The measurements were conducted from 20-800 °C with 5 K/min gradient. Powder X-ray diffraction (PXRD) spectra were recorded on either a D8 Advance (Bruker) or a Rigaku D/max-IIIA diffractometer (Cu Kα, λ = 1.54056 Å) at 293 K. Calculated diffraction patterns of compound **Co_{7+1}** were generated by Mercury. Transmission electron microscopy (TEM) and high-resolution TEM (HR-TEM) images of the samples were obtained using a FEI TalosF 200X transmission electron microscope (200 kV). X-ray photoelectron spectroscopy (XPS) was conducted on VG Microtech ESCA 2000 using a monochromic All X-ray source, and the binding energies (BE) were cali-

brated by setting the measured BE of C 1s to 284.8 eV. The N_2 adsorption-desorption isotherms were collected using a Quantachrome Instruments Autosorb-iQ2-MP at 77 K. Prior to the measurement, the samples were degassed at 200 °C. The surface area of the samples was estimated by method of Brunauer-Emmett-Teller (BET) and the estimation of the distribution of mesoporous and microporous was made by application of the density-functional-theory (DFT) method to the adsorption data. Raman spectra were collected by a Renishaw System 1000 micro-Raman spectroscope.

3. Results and discussion

The novelty of $[Co_7(mmimp)_6(CN)_6]$ $[CoCl_3N(CN)_2]\cdot 3CH_3OH$ is the first presence of μ_3-CN^- bridges at the centre of the Brucite cationic disk (Fig. 1), in place of the usual μ_3-OH, -OCH_3 or -N_3 with retention of the planarity [35,37]. The cyanide exhibits the very rare bonding via the nitrogen atom. The second chemical variation is the co-crystallization with an anion of a cobalt complex. The third is a structural point where the flat cations are not stacked as found in the trigonal symmetry salts but are orthogonal to each other in the orthorhombic space group (*Pbca*) with the counter-anion $[CoCl_3N(CN)_2]^{2-}$ and methanol filling the space in-between.

Although the synthesis was performed under basic conditions, neither OH^- nor OCH_3^- was found because the *in-situ* generated cyanide, presumably from the dicyanamide, is a stronger ligand. All Co^{II} atoms are six-coordinated with near-octahedral geometries and edge-sharing, giving rise to a symmetric coplanar disk. Specifically, the six μ_3-CN bridges the external CoN3O3 octahedral to the central CoN6 one. As found in previous studies, the deprotonated phenolic groups of the six η^1:η^2:η^1:μ_2-bridging Schiff-base ligands connect the periphery of the disks. The six μ_2-O phenolate bridge all outer Co pairs of the hexagon. Consequently, the ligands are tilted alternately away from the disk, three above and three below, looking like a double calix. It should be noted that the cyanide groups as ligands with μ_3-bridged mode were rarely reported, and μ_3-CN bridge ligand in such disks clusters is unprecedented, to the best of our knowledge. The C≡N bond lengths are in the range of 1.12–1.14 Å and the coordination bond lengths involving the Co-N are in the range of 1.94–2.19 Å. IR spectrum of **Co_{7+1}** shows a strong (C≡N) band at 2167 cm^{-1} (Fig. S1 online). Another important part comes from the exotic anion $[CoCl_3N(CN)_2]^{2-}$, which contains three Cl^- and one dicyanamide to form a tetrahedral structure and the anions are "locked" at the edge of the disk $[Co_7]$ through the C-H···N H-bond. The magnetic properties as a function of temperature, field and oscillating frequency indicate the disk behaves as a weakly antiferromagnetically coupled near-neighbour cobalt but with no indication of blocking of the moment down to 2 K (Fig. S2 online).

The thermogravimetry (Fig. 2a) first shows a gradual loss of the methanol followed by a sharp loss of only ca. 12.8% at 310 °C which does not correspond to the destruction of all the organic moiety. Then there is a gradual loss of weight with an anomaly at 500 °C. By monitoring the gases output using a mass spectrometer coupled to the TGA apparatus, the following were identified: CH_4, H_2O, CO, CO_2, HCHO, and CH_3Cl at 290 °C, but only H_2O, CO and CO_2 were found at 500 °C (Fig. 2b). The most striking observation is a depletion of oxygen in the nanostructure upon increasing temperature under argon. The second important observation is the gradual loss between 500 and 800 °C leading to a residue 50.5% of the starting compound at 800 °C. If the final product was Co_3O_4 only 35.4% is expected. These two points led us to explore the products of this thermal degradation as function of temperature—therefore, we prepared samples at 500, 600, 700 and 800 °C for characterization and physical properties evaluation.

It is at an important stage to work out how the degradation proceeds [27,28]. Taking into consideration that dative bonds are weaker than covalent bonds, we may expect the Co-O and Co-N to break before pulverizing the ligands. According to the structure of the cluster and the detected fragments of TG-MS, we can deduce the following three parts (Fig. 2c): (i) the coordination bond between μ_3-CN inner bridge and Co ion may break, then the partial μ_3-CN bridge transfers its charge to Co ions eventually to form cyanide anions or cyanide radicals when the temperature rises from room temperature to 300 °C. (ii) The ether bond with poor stability on the ligand would also be broken in two different ways. On the one hand, the O-C (phenyl) bond is cleaved, accompanied by more HCHO production. On the other hand, the O-C (methyl) bond is cleaved to form CH_4. Meanwhile, the methyl cleavage on the imino group will also produce CH_4. (iii) The chlorine atom of $[CoN(CN)_2Cl_3]^{2-}$ can combine with the methyl group on the nearby ligands to form CH_3Cl, making $\{CoN(CN)_2\}$ an unusually active aggregated centre.

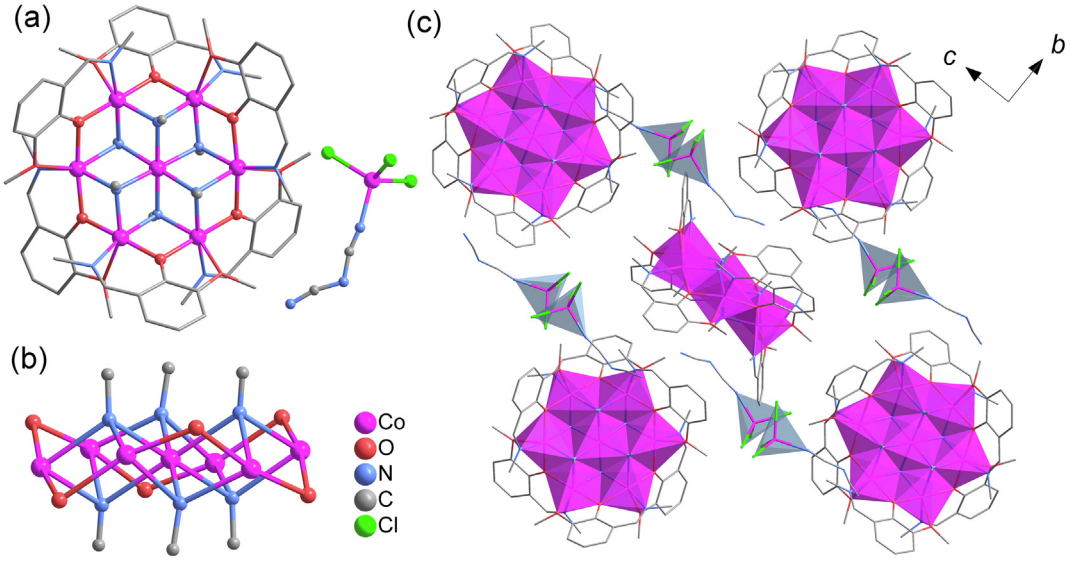

Fig. 1. The structure of **Co_{7+1}**. (a) Molecular structure and (b) core structures of **Co_{7+1}** cluster. (c) Crystal packing of the $[Co_7]$ and $[Co_1]$ unit in the *bc* plane. Hydrogen atoms and solvents and have been omitted for clarity.

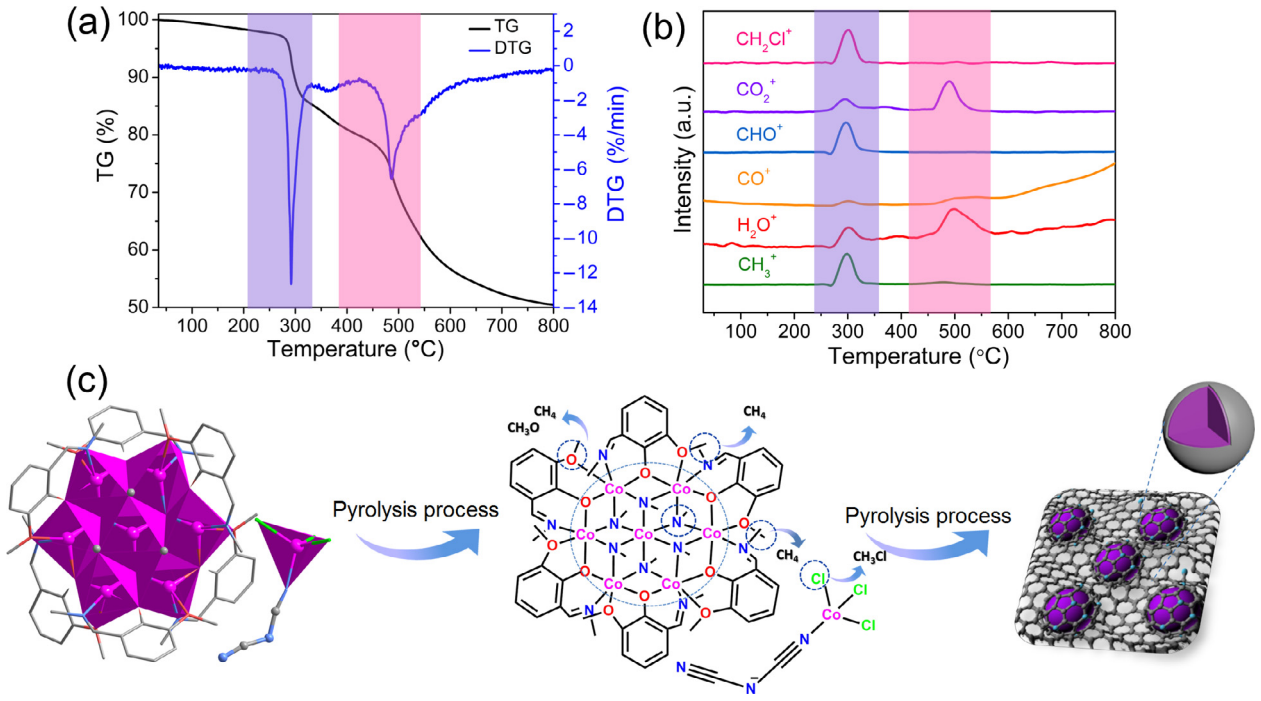

Fig. 2. Tracking the pyrolysis process of **Co_{7+1}**. (a) TG and DTG profile of **Co_{7+1}**. (b) Evolution profiles of the main gaseous decomposition products (*m*/*z* 15, methane; *m*/*z* 18, water; *m*/*z* 28, carbon monoxide; *m*/*z* 29, formyl group; *m*/*z* 44, carbon dioxide; *m*/*z* 50, chloromethane) derived from **Co_{7+1}** pyrolysis process tracking by TG-MS. (c) Possible decomposition and polymerized reaction occurred in pyrolysis process from **Co_{7+1}** to Co@NCs.

Accordingly, the methyl or ether bond on the ligand cleaves to decompose a small organic fragment and also produces a large number of active sites that promote ligand interconnection. The decomposed main ligand can be polymerized by the active sites at its two ends or polymerized with the cyanide group to form a complex carbon network. The decomposed cyanogen can also participate in the fixation and formation of the carbon network by self-polymerization to increase the effective graphite nitrogen content. For instance, as a good active centre, $\{CoN(CN)_2\}$ units are beneficial to connect the skeletons of the surrounding clusters to form higher stability and complex network system. At the same time as the ligand undergoes decomposition and polymerization, the high-valent Co ions of the cluster core and the metal oxide formed with the phenol oxygen are also reduced by adjacent small molecule fragments such as HCHO, CH_4 to form metallic Co accompanied by H_2O, CO and CO_2 evolution, at the same time as the ligand undergoes decomposition and polymerization, and finally to form Co@NC nanostructures. Moreover, fragments such as H_2O, CO and CO_2 were also observed at higher temperatures, which may be due to the rupture and recombination of oxygen functional groups involved in the aromatization process.

In order to clarify the structure of Co@NC, systematic characterizations including PXRD, high-resolution transmission electron microscope (HRTEM) and elemental mapping were performed. The as-synthesized **Co_{7+1}** was pyrolyzed in a low-oxygen-pressure thermo-annealing (Ar-annealing) to prepare the hybrid porous Co@NC-T (T represent the pyrolysis temperature). The presence of the cubic form of metallic cobalt in Co@NC was clearly identified by PXRD (Fig. 3a) with peaks at $2\theta = 44.2°$, 51.6°, and 75.9° assigned respectively to (1 1 1), (2 0 0), and (2 2 0) according to JCPDS No. 15-0806. In contrast, for the two low temperature samples, Co@NC-500 and 600, extra peaks at 41.5° and 47.4° were observed, which can be well indexed to the (1 0 0) and (1 0 1) of hexagonal metallic Co (JCPDS No. 05-0727). Moreover, TEM images of Co@NCs reveal the Co nanoparticles are embedded in a carbon matrix forming homogeneous core-shell structure (Figs. 3c and S3 (online)). To further confirm its phase composition, the HRTEM images of Co@NC-600 (Fig. 3b), demonstrate that the nanoparticle is crystalline, where the Co (1 1 1) crystal plane is clearly seen with a lattice spacing of 0.204 nm, which is consistent with the peak at 44.2° in the PXRD pattern of Co@NC-600. Meanwhile, the spacing of 0.345 nm on the carbon layer can be assigned to the (0 0 2) plane of graphite. Therefore, Co@NC-600 sample has optimized homogeneous core-shell structure compared with other samples. In addition, elemental mapping of Co@NC-600 were conducted as shown in Fig. 3d. For the Co@NC-600 sample, Co and O elements are uniformly distributed in the N doped graphitic carbon structure [41].

For more accurate structural information about the Co@NC materials, XPS, Raman spectra, and the N_2 sorption isotherms have been measured for nanostructures prepared at different pyrolysis temperatures. XPS has been shown to be effective in determining the chemical bonding properties of N, C, O and Co species in catalysts (Table S2 online). The main peaks are centred at 284.6, 398.5, 532.0, and 778.9 eV, and assigned to C 1s, N 1s, O 1s, and Co 2p, respectively (Fig. S4 online). The Co 2p spectrum of the Co@NC-600 sample (Figs. 4a, S5 and Table S3 (online)) shows peaks assigned to Co^0 (778.8 eV), Co-O_x (780.6 eV) and Co-N_x (782.3 eV) [42,43]. The high-resolution N 1s spectrum of Co@NC reveals four types of N species: dominant graphitic-N at 401.3 eV, pyrrolic-N at 400.4 eV, Co-N_x at 399.1 eV, and pyridinic-N at 398.5 eV (Figs. 4b and S6 (online)) [44,45]. In comparison, the resultant core-shell Co@NC-600 presents the optimum percentage of electron-donating graphitic-N (27.5%), electron withdrawing pyridinic-N (25.6%), Co-N interaction (9.3%) and pyrrolic-N (37.6%) (Table S4 online). The deconvolution of the high-resolution C 1s spectrum exhibited three bands, C-C (284.6 eV), C-N or C-O (285.6 eV), C=N or C=O (287.5 eV), respectively (Fig. S7 online). It has been confirmed that the successful bonding of N and O to carbon structure and the C=N can stimulate chemical interaction with nearby metal/carbon atoms to offer active sites [46,47]. In addition, the O 1s spectrum also confirmed the coexistence of oxygen defect

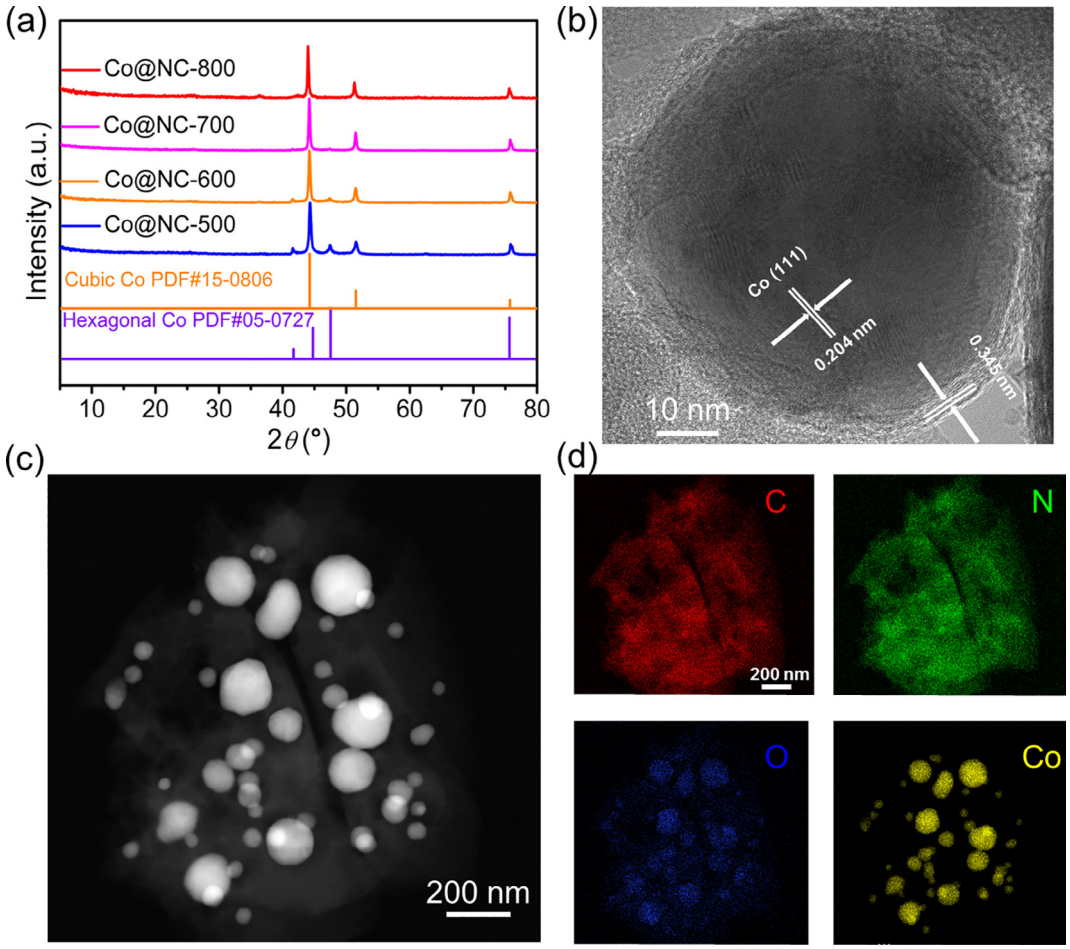

Fig. 3. Structural information of Co@NC nanostructures. (a) Powder XRD patterns of Co@NCs at 500–800. (b–c) HRTEM images and HAADF of Co@NC-600. (d) Elemental mapping images of Co@NC-600 showing the uniform presence of C, N, O and Co.

(531.7 eV), C-O (532.9 eV) and surface oxidation of the metallic cobalt at 530.2 eV, respectively (Fig. S8 online). The Raman spectra of all samples (Fig. 4c) display that five obvious peaks corresponding to Raman active vibrational modes of Co-O and graphite [48]. In detail, peaks at 468.3, 513.4 and 679.7 cm^{-1} are the stretching vibration modes of Co-O and gradually increase with increasing temperature, which is accordance with the XPS analysis. The other two peaks at 1365.5 and 1593.3 cm^{-1} refer to the D (defect) and G (graphite) peaks, further confirming that the carbon skeletons we prepared are graphitized to some extent and have strong electrical conductivity due to the sp^2 graphitic carbon and chaotic or defect carbon, respectively. The intensity ratio of the D to G band (I_D/I_G) rises from 0.69 to 0.94 for Co@NC-500 – 800, indicating that the resulting defects increase underwent higher pyrolysis temperature. As shown in Fig. 4d (Figs. S9, S10, and Table S5 online), The surface area and porosity of the Co@NC nanomaterial were characterized by N_2 sorption isotherms. The large uptake happens at the low relative pressure ($P/P_0 < 0.1$) for all the resulting catalysts, which can be ascribed to the typical I-typed adsorption–desorption phenomena for micropores. Meanwhile, the characteristics of type IV isotherms with a distinct H_3-type hysteresis at high relative pressure ($P/P_0 > 0.5$) indicate the presence of mesopores with a slit shape in the resulting catalysts. The specific surface areas for Co@NC-500, 600, 700 and 800 are 317, 310, 195 and 248 m^3/g based on Brunauer-Emmett-Teller (BET) calculations, respectively. Therefore, all aforementioned characterization clearly suggested that Co@NC-600 sample has optimum percentage of different types of nitrogen, reasonable I_D/I_G ratios and relatively higher surface areas.

In view of the emerging interests in the using nanomaterial containing cobalt for their electrochemical properties for renewable energy and in particular, as electrode in OER, we explore the characteristics of the four samples in search for any correlation with the characteristics discussed above. We deposited an even layer of the nanoparticles onto a carbon paper for electrochemistry in 1 mol/L KOH with particular attention to the overpotential, Tafel slope, double-layer capacitance (C_{dl}) which is linearly proportional to electrochemical surface area (ECSA), and EIS. All indicate an optimum quality performance for the sample prepared at 600 °C.

The overpotential at the current density of 10 mA/cm^2 is the lowest at 257 mV compared to 345 mV for Co@NC-500, 285 mV for Co@NC-700, 318 mV for Co@NC-800, and 320 mV for RuO_2 (Fig. 5a). The Tafel slope is also lowest at 86.2 mV/dec for Co@NC-600 compared to 111.6, 99.3, and 119.9 mV/dec for Co@NC-500, Co@NC-700 and Co@NC-800, respectively (Fig. 5b). Thus, a speedier OER rates for Co@NC-600 is useful for practical application as electrocatalyst. The combined overpotential vs. Tafel plot (Fig. 5c) highlights the superior OER performance of the Co@NC-600 electrode. The results indicated that Co@NC-600 has excellent electrocatalytic performance, which is comparable to the state-of-the-art Co-based electrocatalyst (Table S6 online). The electrochemical double-layer capacitance, which is linearly proportional to the ECSA, is 77.4 mF/cm^2 for Co@NC-600. It exceeds those for Co@NC-500, Co@NC-700 and Co@NC-800, by a staggering

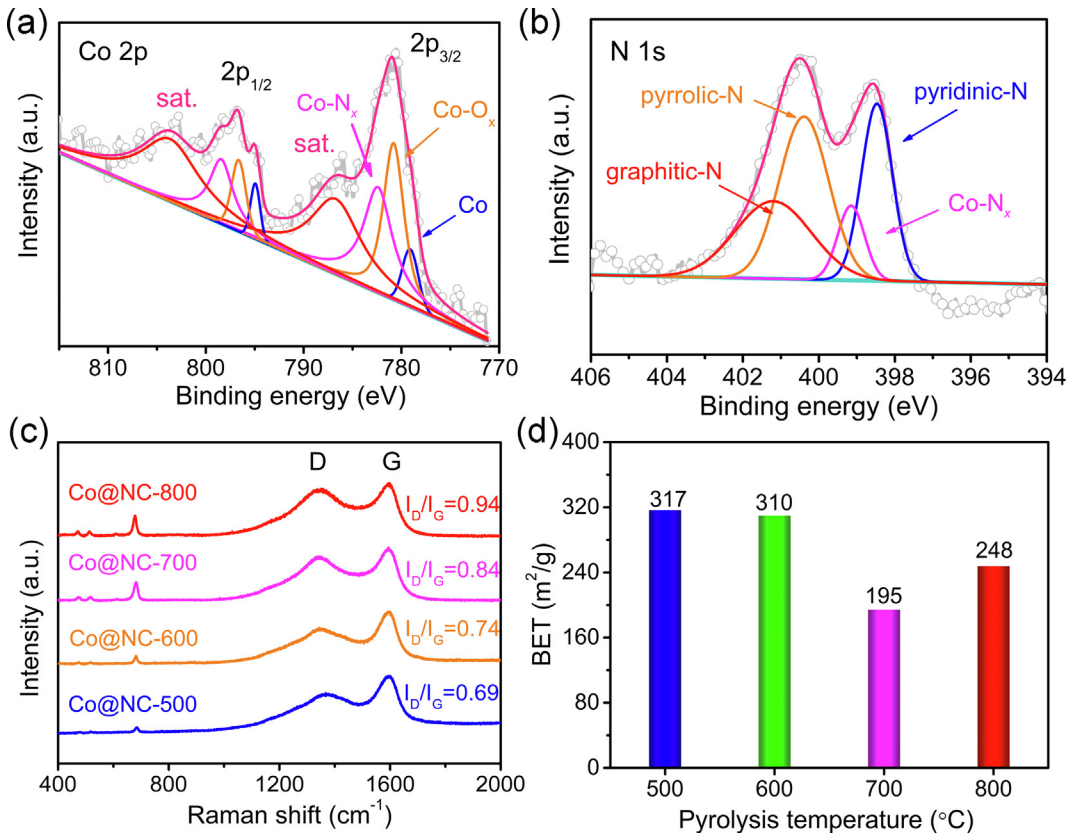

Fig. 4. The chemical bonding environment of Co@NC nanostructures. (a) XPS survey spectrum of the Co@NC-600 for Co 2p. (b) XPS survey spectrum of the Co@NC-600 for N 1s. (c) Raman spectroscopy of Co@NCs. (d) Brunauer-Emmett-Teller (BET) values of all Co@NC materials.

26.1, 67.8, 43.4 mF/cm^2, respectively (Figs. 5d and S10 (online)). EIS provides information of the electrode kinetics. The Nyquist plots (Fig. 5e) show a clear effect—wide to narrow dependence $-Z_{Im}$ vs. Z_{Re} in the order Co@NC-500 > Co@NC-800 > Co@NC-700 > Co@NC-600, this is due to the fact that Co@NC-600 (R_{ct} = 5.47 Ω) has a smaller charge transfer resistance than other electrocatalysts (R_{ct}, 13.1 Ω for Co@NC-500, 7.67 Ω for Co@NC-700 and 11.22 Ω for Co@NC-800). The measured impedance spectra data were fitted using Zview software shows that is the equivalent circuit in the form of R_s (CPE1, R_o) (CPE2, R_{ct}). And R_o is oxide film resistance and R_{ct} denotes the charge transfer resistance at catalyst/electrolyte interface [49]. The charge transfer resistance of the electrode is closely related to the electron transport rate in the OER catalytic process. The minimum charge transfer resistance indicates the best OER performance for Co@NC-600. In order to study the stability for Co@NC-600 at electrocatalysis process, the chronopotentiometry was conducted in O_2-saturated 1.0 mol/L KOH solutions. As shown in Fig. 5f, only a marginal increase of potential results long-term stability test after 15 h of Co@NC-600 electrode at a current density of 10 mA/cm^2. Furthermore, the PXRD patterns of Co@NC-600 before and after catalysis showed the same corresponding peaks, indicating that the phase did not change after catalysis (Fig. S11 online). In addition, through the comparison of TEM of Co@NC-600 before and after catalysis, it was found that the morphology of the samples also did not change, and the core-shell nanostructures were still maintained. The above indicates that the Co@NC-600 has excellent stability for OER in alkaline media. The enhanced electrocatalytic activity of Co@NC-600 for OER might be ascribed to the following aspects: (i) the core-shell structured Co@NC-600 with higher electrochemical surface area can endow more electrolyte/electrode contact area for the electrocatalytic reaction; (ii) the existence of carbon shell in Co@NC-600 could improve the charge transfer efficiency and electrical conductivity, which was proved by EIS measurement; (iii) the carbon shell could prevent cobalt particles from agglomeration, thus provide more active sites for the catalytic process.

4. Conclusions

In summary, a novel co-crystalline cluster $[Co^{II}_7(\mu_3\text{-}CN)_6(mmimp)_6]$ $[Co^{II}Cl_3N(CN)_2]\cdot 3CH_3OH$ having a unique Brucite disk with *in-situ* generated μ_3-CN bridge was obtained and packed orthogonally. The decomposition of dicyanamide avoids the direct use of highly toxic cyanide. Its low oxygen content proceeds with a gradual thermal decomposition under inert atmosphere to Co@NC nanostructures, which is tracked and systematically analysed by TG-MS. The products, identified by microscopy and diffraction, consist of metallic cobalt core and N-doped carbon shell. In particular, the most astonishing is their performance as OER electrode being optimum for the sample prepared at 600 °C which achieves an ultralow overpotential of 257 mV at a current density of 10 mA/cm^2. As a result, it is the first time to use nitrogen-rich coordination cluster as precursor for controlled pyrolysis to achieve high OER performance where TG-MS technique was used to determine the best pyrolysis condition. This new method of controlled pyrolysis from distinct molecular clusters to core-shell nanostructure offers a prototype from coordination chemistry to nanomaterials for energy conversion through precisely pyrolysis tracking and control.

Conflict of interest

The authors declare that they have no conflict of interest.

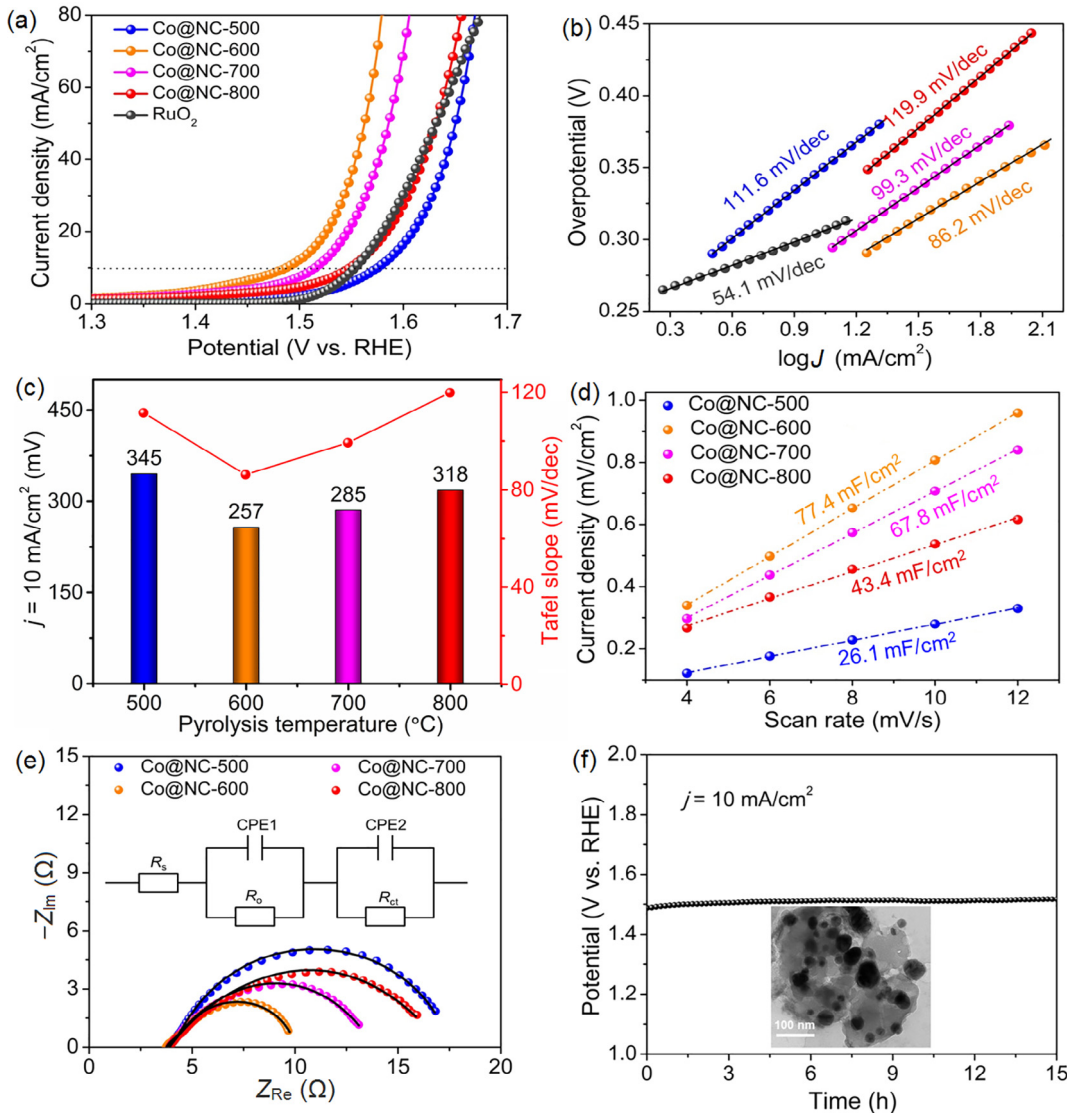

Fig. 5. OER activity of Co@NC nanostructures. (a) IR-corrected polarization LSV curves in 1 mol/L KOH solution. (b) Corresponding Tafel plots. (c) Comparison of overpotentials at j = 10 mA/cm^2 corresponds to Tafel slopes. (d) Current density as a function of the scan rate for all as-obtained electrodes. (e) Nyquist plots of catalysts at the biased potential of 1.6 V vs. RHE over the frequency range from 10,000 to 0.01 Hz. (f) Chronopotentiometric measurements of long-term stability of Co@NC-600. The inset shows the TEM image after OER test, scale bar is 100 nm.

Acknowledgments

This work was supported by the National Natural Science Foundation of China for Distinguished Young Scholars (21525101), the BAGUI Talent Program and Scholar Program (2014A001), the National Natural Science Foundation of China (21805074 and 21661008), the Natural Science Foundation of Hubei Province (2017CFA006 and 2018CFB151), the Natural Science Foundation of Guangxi Zhuang Autonomous Region (2017GXNSFDA198040). MK is supported by the Centre National de la Recherche Cientifique (CNRS, France).

Author contributions

Ming-Hua Zeng conceived the idea, co-wrote the paper and supervised the whole experimental procedure and data analysis. Mohamedally Kurmoo and Xu Peng edited the manuscript. Jian-Qiang Zhao, Dandan Cai, Jun Dai and Xu Peng performed the experiments, analyzed the data and wrote the manuscript. All the authors discussed the results, commented on and revised the manuscript.

Appendix A. Supplementary materials

Supplementary materials to this article can be found online at https://doi.org/10.1016/j.scib.2019.09.013.

References

[1] You B, Sun Y. Innovative strategies for electrocatalytic water splitting. Acc Chem Res 2018;51:1571–80.
[2] Cao X, Tan C, Sindoro M, et al. Hybrid micro-/nano-structures derived from metal–organic frameworks: preparation and applications in energy storage and conversion. Chem Soc Rev 2017;46:2660–77.
[3] Hunter BM, Gray HB, Muller AM. Earth-abundant heterogeneous water oxidation catalysts. Chem Rev 2016;116:14120–36.
[4] Xiao P, Chen W, Wang X. A review of phosphide-based materials for electrocatalytic hydrogen evolution. Adv Energy Mater 2015;5:1500985.
[5] Zhang X, Chang L, Yang Z, et al. Facile synthesis of ultrathin metal–organic framework nanosheets for Lewis acid catalysis. Nano Res 2019;12:437–40.
[6] Han J, An P, Liu S, et al. Reordering d-orbital energies of single-site catalysts for CO_2 electroreduction. Angew Chem Int Ed 2019;58:12711–6.
[7] Chen P, Zhou T, Chen M, et al. Enhanced catalytic activity in nitrogen-anion modified metallic cobalt disulfide porous nanowire arrays for hydrogen evolution. ACS Catal 2017;7:7405–11.

[8] Tong Y, Chen P, Zhou T, et al. A bifunctional hybrid electrocatalyst for oxygen reduction and evolution: cobalt oxide nanoparticles strongly coupled to B, N-decorated graphene. Angew Chem Int Ed 2017;56:7121–5.
[9] Zhang B, Zheng X, Voznyy O, et al. Homogeneously dispersed multimetal oxygen-evolving catalysts. Science 2016;352:333–7.
[10] Yang Y, Lin Z, Gao S, et al. Tuning electronic structures of nonprecious ternary alloys encapsulated in graphene layers for optimizing overall water splitting activity. ACS Catal 2017;7:469–79.
[11] Long C, Li X, Guo J, et al. Electrochemical reduction of CO_2 over heterogeneous catalysts in aqueous solution: recent progress and perspectives. Small Methods 2019;3:1800369.
[12] Zheng Y, Jiao Y, Vasileff A, et al. The hydrogen evolution reaction in alkaline solution: from theory, single crystal models, to practical electrocatalysts. Angew Chem Int Ed 2018;57:7568–79.
[13] Gao S, Lin Y, Jiao X, et al. Partially oxidized atomic cobalt layers for carbon dioxide electroreduction to liquid fuel. Nature 2016;529:68–71.
[14] Cai G, Zhang W, Jiao L, et al. Template–directed growth of well-aligned MOF arrays and derived self-supporting electrodes for water splitting. Chem 2017;2:791–802.
[15] Li X, Wei J, Li Q, et al. Nitrogen-doped cobalt oxide nanostructures derived from cobalt-alanine complexes for high-performance oxygen evolution reactions. Adv Funct Mater 2018;28:1800886.
[16] Seh ZW, Kibsgaard J, Dickens CF, et al. Combining theory and experiment in electrocatalysis: Insights into materials design. Science 2017;355:eaad4998.
[17] Zhang H, Nai J, Yu L, et al. Metal–organic-framework-based materials as platforms for renewable energy and environmental applications. Joule 2017;1:77–107.
[18] Chen YZ, Zhang R, Jiao L, et al. Metal–organic framework-derived porous materials for catalysis. Coord Chem Rev 2018;362:1–23.
[19] Zhao S, Wang Y, Dong J, et al. Ultrathin metal–organic framework nanosheets for electrocatalytic oxygen evolution. Nat Energy 2016;1:16184–94.
[20] Zheng Y, Cheng P, Xu J, et al. MOF-derived nitrogen-doped nanoporous carbon for electroreduction of CO_2 to CO: the calcining temperature effect and the mechanism. Nanoscale 2019;11:4911–7.
[21] Chen H, Shen K, Mao Q, et al. Nanoreactor of MOF-derived yolk-shell Co@ C-N: precisely controllable structure and enhanced catalytic activity. ACS Catal 2018;8:1417–26.
[22] Xu YT, Ye ZM, Ye JW, et al. Non-3d metal modulation of a cobalt imidazolate framework for excellent electrocatalytic oxygen evolution in neutral media. Angew Chem Int Ed 2019;58:139–43.
[23] Wang X, Xiao H, Li A, et al. Constructing NiCo/Fe_3O_4 heteroparticles within MOF-74 for efficient oxygen evolution reactions. J Am Chem Soc 2018;140:15336–41.
[24] Chu Y, Guo L, Xi B, et al. Embedding MnO@Mn_3O_4 nanoparticles in an N-dope-carbon framework derived from Mn-organic clusters for efficient lithium storage. Adv Mater 2018;30:1704244.
[25] Shi C, Chen M, Han X, et al. Thiacalix [4] arene-supported tetradecanuclear cobalt nanocage cluster as precursor to synthesize CoO/Co_9S_8@CN composite for supercapacitor application. Inorg Chem Front 2018;5:1329–35.
[26] Du J, Liu G, Li F, et al. Iron-salen complex and Co^{2+} ion-derived cobalt-iron hydroxide/carbon nanohybrid as an efficient oxygen evolution electrocatalyst. Adv Sci 2019;6:1900117.
[27] Lee KJ, Lee JH, Jeoung S, et al. Transformation of metal–organic frameworks/coordination polymers into functional nanostructured materials: experimental approaches based on mechanistic insights. Acc Chem Res 2017;50:2684–92.
[28] Zhang L, Hu YH. A systematic investigation of decomposition of nano $Zn_4O(C_8H_4O_4)_3$ metal–organic framework. J Phys Chem C 2010;114:2566–72.
[29] Yin Z, Wang QX, Zeng MH. Iodine release and recovery, influence of polyiodide anions on electrical conductivity and nonlinear optical activity in an interdigitated and interpenetrated bipillared-bilayer metal–organic framework. J Am Chem Soc 2012;134:4857–63.
[30] Sun F, Yin Z, Wang QQ, et al. Tandem postsynthetic modification of a metal–organic framework by thermal elimination and subsequent bromination: effects on absorption properties and photoluminescence. Angew Chem Int Ed 2013;52:4538–43.
[31] Zeng MH, Yin Z, Tan YX, et al. Nanoporous cobalt (II) MOF exhibiting four magnetic ground states and changes in gas sorption upon post-synthetic modification. J Am Chem Soc 2014;136:4680–8.
[32] Zeng MH, Yin Z, Liu ZH, et al. Assembly of a highly stable luminescent Zn_5 cluster and application to bio-imaging. Angew Chem Int Ed 2016;55:11407–11.
[33] Hu YQ, Zeng MH, Zhang K, et al. Tracking the formation of a polynuclear Co_{16} complex and its elimination and substitution reactions by mass spectroscopy and crystallography. J Am Chem Soc 2013;135:7901–8.
[34] Zhang M, Yang T, Wang Z, et al. Chemical reaction within a compact non-porous crystal containing molecular clusters without the loss of crystallinity. Chem Sci 2017;8:5356–61.
[35] Zhou Y, Zeng MH, Wei LQ, et al. Traditional and microwave-assisted solvothermal synthesis and surface modification of Co_7 brucite disk clusters and their magnetic properties. Chem Mater 2010;22:4295–303.
[36] Zheng HL, Chen XL, Li T, et al. Manipulating clusters by use of competing N, O-chelating ligands: a combined crystallographic, mass spectrometric, and DFT study. Chem Eur J 2018;24:7906–12.
[37] Cai D, Han A, Yang PY, et al. Heptanuclear Co, Ni and mixed Co-Ni clusters as high-performance water oxidation electrocatalysts. Electrochim Acta 2017;249:343–52.
[38] Na HX, Yang PY, Yin Z, et al. Stepwise assembly of M_7^{II} clusters revealed by mass spectrometry, EXAFS, and crystallography. Chem Eur J 2016;22:18404–11.
[39] Pan B, Peng X, Wang Y, et al. Tracking the pyrolysis process of a 3-MeOsalophen-ligand based CO_2 complex for promoted oxygen evolution reaction. Chem Sci 2019;10:4560–6.
[40] Sheldrick GM. Crystal structure refinement with SHELXL. Acta Crystallogr Sect C Struct Chem 2015;71:3–8.
[41] Jin H, Wang J, Su D, et al. *In situ* cobalt-cobalt oxide/N-doped carbon hybrids as superior bifunctional electrocatalysts for hydrogen and oxygen evolution. J Am Chem Soc 2015;137:2688–94.
[42] Li Y, Jia B, Fan Y, et al. Bimetallic zeolitic imidazolite framework derived carbon nanotubes embedded with Co nanoparticles for efficient bifunctional oxygen electrocatalyst. Adv Energy Mater 2018;8:1702048.
[43] Cai S, Wang R, Yourey WM, et al. An efficient bifunctional electrocatalyst derived from layer-by-layer self-assembly of a three-dimensional porous Co-NC@ graphene. Sci Bull 2019;64:968–75.
[44] Chen YZ, Wang C, Wu ZY, et al. From bimetallic metal–organic framework to porous carbon: high surface area and multicomponent active dopants for excellent electrocatalysis. Adv Mater 2015;27:5010–6.
[45] Chen Z, Wang Q, Zhang X, et al. N-doped defective carbon with trace Co for efficient rechargeable liquid electrolyte-/all-solid-state Zn-air batteries. Sci Bull 2018;63:548–55.
[46] Sivanantham A, Ganesan P, Estevez L, et al. Water electrolysis: a stable graphitic, nanocarbon-encapsulated, cobalt-rich core-shell electrocatalyst as an oxygen electrode in a water electrolyzer. Adv Energy Mater 2018;8:1702838.
[47] Guo S, Yang Y, Liu N, et al. One-step synthesis of cobalt, nitrogen-codoped carbon as nonprecious bifunctional electrocatalyst for oxygen reduction and evolution reactions. Sci Bull 2016;61:68–77.
[48] Sivanantham A, Ganesan P, Estevez L, et al. A stable graphitic, nanocarbon-encapsulated, cobalt–rich core–shell electrocatalyst as an oxygen electrode in a water electrolyzer. Adv Energy Mater 2018;8:1702838.
[49] Zhang J, Li F, Chen W, et al. Facile synthesis of hollow Co_3O_4-embedded carbon/reduced graphene oxides nanocomposites for use as efficient electrocatalysts in oxygen evolution reaction. Electrochim Acta 2019;300:123–30.

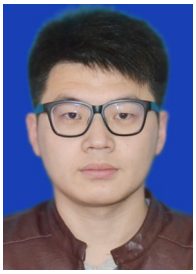

Jian-Qiang Zhao joined Prof. Ming-Hua Zeng's group as a Master's student at Guangxi Normal University and has received his M.S. degree in 2019. His research is focused on 3d-coordination clusters, especially their synthesis and pyrolysis leading to nanomaterials with electrocatalysis properties.

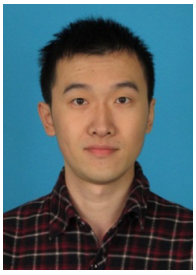

Xu Peng obtained his Ph.D. degree in Inorganic Chemistry at University of Science and Technology of China in 2017. He currently works at College of Chemistry and Chemical Engineering as associate professor, Hubei University. His research is focused on controlled pyrolysis of the low-dimensional 3d metal solid for their applications in energy storage and conversion areas.

Ming-Hua Zeng obtained his Ph.D. degree from Sun Yat-sen University in 2004. Then he started his individual research in Guangxi Normal University and obtained the position of full professor in 2006. His earlier research focused on the synthesis, properties, structural transformation and post-synthetic modification of coordination clusters and metal–organic frameworks. Currently his interest has turned to the coordination molecular cluster chemistry in solution as well as their assembly processing, mechanism and application.